AIAA JOURNAL
Vol. 44, No. 4, April 2006

Aerodynamics of Recirculating Flow Control Devices for Normal Shock/Boundary-Layer Interactions

K. R. Srinivasan,* E. Loth,† and J. C. Dutton‡
University of Illinois at Urbana–Champaign, Urbana, Illinois 61801

Passive methods of controlling shock/boundary-layer interactions (SBLIs) consist of a porous surface covering a cavity or a plenum located in the region of the SBLI. The present study focuses on the flowfield downstream of a Mach 1.42 SBLI controlled with various passive devices such as a conventional porous plate, a microporous plate, streamwise slots, a conventional mesoflap array, and a hybrid flap array. Qualitative analysis of the flowfield for the various control devices investigated was achieved with spark shadowgraph visualizations and surface oil-flow visualizations. Quantitative analysis was accomplished by measuring surface static pressure distributions and boundary layer velocity profiles. The flowfields downstream of the slot-controlled and hybrid flap array–controlled SBLIs were found to be highly three-dimensional, whereas the flowfields were predominantly two-dimensional for the remainder of the control devices. It was found that only the conventional mesoflap array had an improved total pressure recovery compared to the baseline solid wall.

Nomenclature

H	=	shape factor
P	=	static pressure
P_t	=	total pressure
P_0	=	stagnation chamber pressure
Re	=	Reynolds number
U	=	streamwise velocity
U_0	=	incoming freestream streamwise velocity
X^*	=	nondimensional streamwise distance, $(x - x_0)/\delta_0$
x	=	streamwise distance
x_0	=	streamwise distance to center of cavity
Y^*	=	nondimensional transverse distance, y/δ_0
y	=	transverse (wall-normal) distance from bottom of channel
Z^*	=	nondimensional spanwise distance, z/δ_0
z	=	spanwise distance from channel midplane
α	=	stagnation pressure recovery factor
δ_0	=	incoming boundary layer thickness
δ^*	=	displacement thickness
δ_0^*	=	incoming displacement thickness
θ	=	momentum thickness
θ_0	=	incoming momentum thickness

Introduction

NORMAL shock/boundary-layer interactions (SBLIs) occur in a number of important high-speed flow applications such as turbomachines, transonic and supersonic flow over wings, and supersonic flow through aircraft inlet systems. The present investigation deals with the interaction of normal shock waves and boundary layers as occurs in supersonic inlets. Such interactions can have a major impact on the inlet efficiency of supersonic vehicles, because they can cause significant stagnation pressure losses and flow nonuniformities. It is therefore imperative that the interactions be controlled in order to improve supersonic inlet performance.

A traditional method of controlling shock/boundary layer interactions involves "bleeding" of the low-momentum fluid in the boundary layer downstream of the interaction. Boundary layer bleed is currently employed in aircraft cruising at Mach 2 and above.[1] Bleeding prevents boundary layer separation and increases the flow uniformity, but incurs major penalties. The drag on the aircraft increases as the size and weight of the inlet increase to accommodate the ducting for the bled-off air. The inlet size (capture area) and weight of the inlet are also increased to compensate for the mass of bled-off air. Thus, it would be advantageous to employ an SBLI control system without bleed that is capable of maintaining the same or improved inlet performance.

Recirculating Control Studies

Many previous research efforts[2–8] on controlling shock/boundary layer interactions have investigated recirculating flow techniques. These passive control methods consist of a porous surface covering a cavity or plenum located in the region of the SBLI. Recent passive control studies also include the use of streamwise slots[9] instead of the conventional porous surface–type passive control. The static pressure rise across the shock wave results in a flow through the cavity from downstream to upstream of the shock. Experimental studies have shown that cavity recirculation can have a positive impact on total pressure recovery, thereby improving wave drag. However, these studies have also shown that this passive control method can detrimentally affect boundary layer displacement and momentum thicknesses, resulting in an increase in viscous drag. Thus, the potential benefit of passive (recirculating) control lies in the delicate balance between these two opposing tendencies.

A novel concept termed MART (mesoflaps for aeroelastic recirculating transpiration), developed at the University of Illinois, aims to exploit the "lambda shock benefit" as much as possible, while minimizing the viscous drag increase, so that the overall total pressure recovery is increased compared to that for the solid wall. Its application in supersonic inlets also necessitates the minimization of flow distortion and shock oscillations.

The MART system consists of a matrix of flaps covering an enclosed cavity as shown in Fig. 1a. Each of the flaps is rigidly fixed over a small portion of its upstream end, but can aeroelastically deflect at its downstream end, based on the pressure difference between the supersonic flow above and the subsonic cavity flow below. This allows for downstream removal of the low-momentum portion of the boundary layer, in a fashion similar to conventional boundary layer bleed. Upstream of the shock, however, the flaps deflect upward

Presented as Paper 2004-0426 at the 42nd Aerospace Sciences Meeting, Reno, NV, 5–8 January 2004; received 1 September 2004; revision received 20 September 2005; accepted for publication 29 September 2005.

*Graduate Research Assistant, Department of Aerospace Engineering.
†Professor, Department of Aerospace Engineering. Associate Fellow AIAA.
‡Professor, Department of Mechanical and Industrial Engineering. Associate Fellow AIAA.

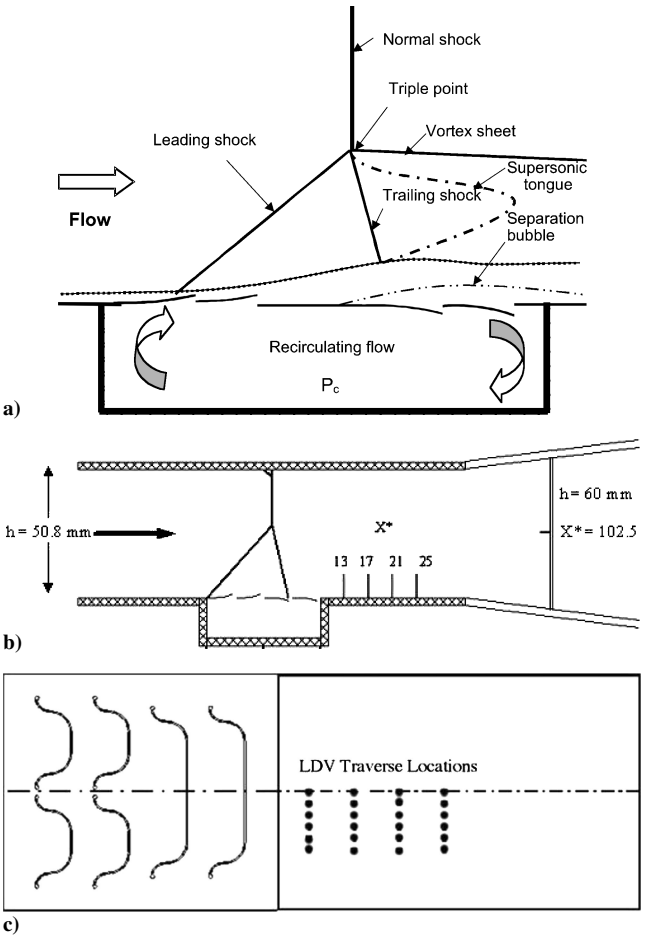

Fig. 1 Schematic of a) the MART concept, b) wind-tunnel test section and diffuser showing the measurement locations, c) LDV traverse locations on the tunnel bottom wall.

into the low-pressure region preceding the shock system. The flow bled off through the downstream flaps is reinjected through these upstream flaps.

The MART concept possesses several potential advantages over conventional passive control. Assuming that flap deflections are kept relatively small (i.e., below the sonic line of the boundary layer), the MART arrays allow for nearly tangential bleed and injection, thereby providing an aerodynamic advantage over the more transversely oriented bleed and injection associated with conventional passive control. Also, the flap deflections into the oncoming supersonic flow form leading oblique shocks. These shocks essentially replace the stronger normal shock (with no control) and help reduce total-pressure losses across the SBLI. This is the lambda shock benefit referred to earlier. In addition, the flaps are aerodynamically activated, since they can deflect only when a shock is present. They can therefore adjust to complex shock-system topology and shock movement because any change in the shock-system location changes the pressure loading on the flap array, which, in turn, alters flap deflections. Under subsonic conditions, the flaps revert to a nearly smooth solid wall, thereby minimizing the roughness (and increase in friction drag) associated with conventional passive control techniques at off-design conditions.

Hafenrichter et al.[10] studied four-flap and six-flap arrays of varying thicknesses, with the four-flap arrays generally outperforming the six-flap arrays. Orphanides[11] modified the geometry of the four-flap arrays to consist of S-curve shapes and found an optimal array thickness for total pressure recovery. The present work expands upon this by experimentally studying the three-dimensional flowfield downstream of the SBLI for the optimal MART array[11] and comparing it with the flowfields for various other passive control devices including macroporous, microporous, streamwise slot, and hybrid flap array control devices. Spark shadowgraph visualizations, surface oil-flow visualizations, surface static pressure distributions, and measurements of boundary layer mean velocity profiles are presented.

Description of Facility and Experimental Methods

Facility

The supersonic blowdown wind tunnel is fed compressed air by a Model SSR HPE 300 Ingersoll–Rand compressor, capable of delivering air at 965 kPa and 0.74 kg/s. The compressed air is desiccated and made contaminant-free as it passes through a series of filters, driers, and coolers. The air then pressurizes a tank farm with a volume of approximately 140 m^3. The tunnel stagnation pressure is controlled by a Fisher TL101 Process Controller, which actuates a control valve by supplying a 4–20-mA signal. A pressure transducer measures the pressure in the stagnation chamber and sends a 0–5-V output to the controller, which then automatically controls the stagnation pressure.

The pressurized air passes through facility flow-conditioning devices and enters the stagnation chamber, where it is slowed to low subsonic speeds. The tunnel stagnation temperature is measured using an Omega Chromega–Alomega (type K) grounded thermocouple. The stagnation temperature for all the experiments was measured at 297 ± 3 K. The converging–diverging (C–D) nozzle accelerates the flow into a 50.8×50.8 mm test section. A uniform flow is created at the exit of the C–D nozzle, where the flow reaches a Mach number of 1.42 ± 0.02. The test section has optical access on two sides, wherein a part of the tunnel sidewalls is fitted with removable fused silica windows. All the experiments were performed at an absolute stagnation pressure of approximately 129 kPa, which corresponds to a unit Reynolds number of $18 \times 10^6\ m^{-1}$. Further descriptions of the complete experimental setup, including the downstream subsonic diffuser, can be found in Ref. 12.

Diagnostic Techniques

Spark shadowgraphs were obtained on Polaroid 55 land film using a Xenon Model 457 micropulser as the light source with a spark duration of 1.4 μs. The micropulser emits a spark of light through a 1.5-mm aperture that is positioned at the focal length of a concave mirror of diameter 29.4 cm and focal length 162.6 cm. As a result, collimated light enters the test section in a direction orthogonal to the flow direction. The Polaroid film is placed on a Polaroid Model 545i 9×12 cm film holder and is kept 15–20 cm from the fused silica windows of the test section. Shadowgraphs were obtained for all the experimental cases including the baseline solid-wall case.

Qualitative surface-flow measurements were also carried out using oil-streak visualizations. The oil streaklines can be used to estimate the location and extent of separation. The accumulation of oil in various regions of the flowfield indicates the presence of flow separation or regions of low wall shear stress. The oil-streak visualizations also serve as a tool to examine the two dimensionality or asymmetries in the flow. A mixture of carbon black and kerosene was used as the surface tracer.[13] The mixture was thinned with STP oil treatment and acetone. The process was repeated until the desired viscosity for the mixture was obtained. Finally, two drops of a fluorescent dye were added as a marker, in order to more easily trace the surface streaklines.

A total of 40 static pressure taps are located along the spanwise centerline of the bottom wall of the test section. Fourteen of these taps are located upstream of the cavity, 13 taps along the cavity bottom, and 13 taps downstream of the cavity. Each tap has a diameter of 400 μm, and the taps are placed 3.18 mm apart. In the subsonic diffuser (Fig. 1b), 23 static pressure taps are located along the spanwise centerline; the first tap is located 28.6 mm from the entrance of the diffuser. The spacing between the first two taps is 17.15 mm while the rest of the taps are placed 19.05 mm apart. Fourteen pressure taps are located across the span of the test section, at a distance of 57 mm (downstream) from the center of the cavity. The spanwise taps are placed 3.125 mm apart. The accuracy of the static pressure measurements is $\pm 0.05\%$ of the full-scale reading.

Laser Doppler velocimetry (LDV) was used to measure the boundary layer profiles upstream and downstream of the interaction. A one-component streamwise LDV setup was used in order to obtain high spatial resolution near the wall. The laser used was a Spectra-Physics Stabilite 2017-06S continuous wave argon-ion laser capable of outputting up to 6 W. The laser produces a multiline beam consisting of green (514.5-nm), blue (488-nm), and violet (476.5-nm) light. The multiline beam is then split into pairs of the three colored components using a TSI Model 9201 ColorBurst multicolor beam separator. Fiber-optic couplers are used to transmit the beams to the Model 9253-500 fiber-optic probe (the transmitting probe). The receiving optics capture the scattered light from the probe volume and transmit it to the Model 9230 ColorLink Plus multicolor receiver. The resulting light signals are converted to voltage signals and are passed on to the Model 750 IFA digital burst correlator, in which the Doppler frequency and velocity data are extracted. The silicone oil used for the LDV seed particles in the experiments had a viscosity of 50 cP and a specific gravity of 0.96. The polydispersed silicone oil droplets have a mean diameter of approximately 0.8 μm and have been found in previous studies to follow turbulent flow fluctuations of frequencies of at least 30 kHz and, perhaps, even above 200 kHz (Refs. 14 and 15). Particle lag effects are confined to regions of a few millimeters downstream of the shock waves, as shown by previous measurements.[14] Wall-normal boundary layer traverses were performed at 24 locations in the test section. The measurements were obtained at four streamwise locations and six spanwise locations; see Fig. 1c. Measurements were obtained on one side of the centerline, and the farthest outboard spanwise location is halfway between the sidewalls and the centerline. Each wall-normal boundary layer traverse consists of approximately 60 measurement locations. The overall maximum mean-velocity uncertainty is 2.1% of the incoming freestream velocity U_0.

Finally, pitot pressure profiles were obtained in the subsonic diffuser using a flat-head pitot probe; see Fig. 1b for the location of the diffuser pitot pressure profiles. The probe was inserted through slots machined in the diffuser top and bottom walls and was attached to a traverse system. The total uncertainty of the measured total pressure in the diffuser was evaluated to be between 0.95 and 1.2% of the stagnation chamber pressure.

Test Cases

The macroporous plate represents a conventional passive control method, and the holes in the plate result in an effective porosity of 5%, which is consistent with typical bleed porosity for conventional passive control methods and hole sizes (when normalized by the incoming displacement thickness, as mentioned in Refs. 3 and 4). The plate consists of 81 1.32-mm-diam holes arranged in nine rows. Figure 2a displays a schematic of the conventional porous surface. The streamwise spacing of the holes is 4.67 mm, and the spanwise spacing is 5.08 mm. The holes are arranged in a staggered manner, as can be seen in the schematic. The end with the set of five holes is placed upstream (rather than the end with four holes) to generate a stronger lambda shock.

The microporous plate or microporous skin has an overall porosity of 4%. This porosity is achieved through numerous microholes located across the surface of the plate. The microporous skin is a Northrop Grumman nickel plate, termed GAC1897, with hourglass-shaped holes. The skin is 305 μm thick and has 60-μm-throat-diameter holes. The porosity percentage based on the openings at the skin surface is 50%, but is only 4% open based on the throat diameter.

The streamwise slots (Fig. 2b) consist of three slots (41 mm long $\times$ 1.8 mm wide $\times$ 0.25 mm deep) with one slot located along the centerline of the test section, and the other two slots placed symmetrically on either side of the centerline. The centerlines of the slots are separated by a distance of 10.16 mm.

To promote streamwise vorticity, a hybrid flap array was designed, which consisted of six flaps arranged in four rows as shown in Fig. 2d. The hybrid flaps are aligned in such a way that the outer S-curves of the smaller flaps coincide with the outer S-curves of the conventional four-flap array (Fig. 2c). The thickness of the hybrid flaps is 152 μm, as for the conventional four-flap array.

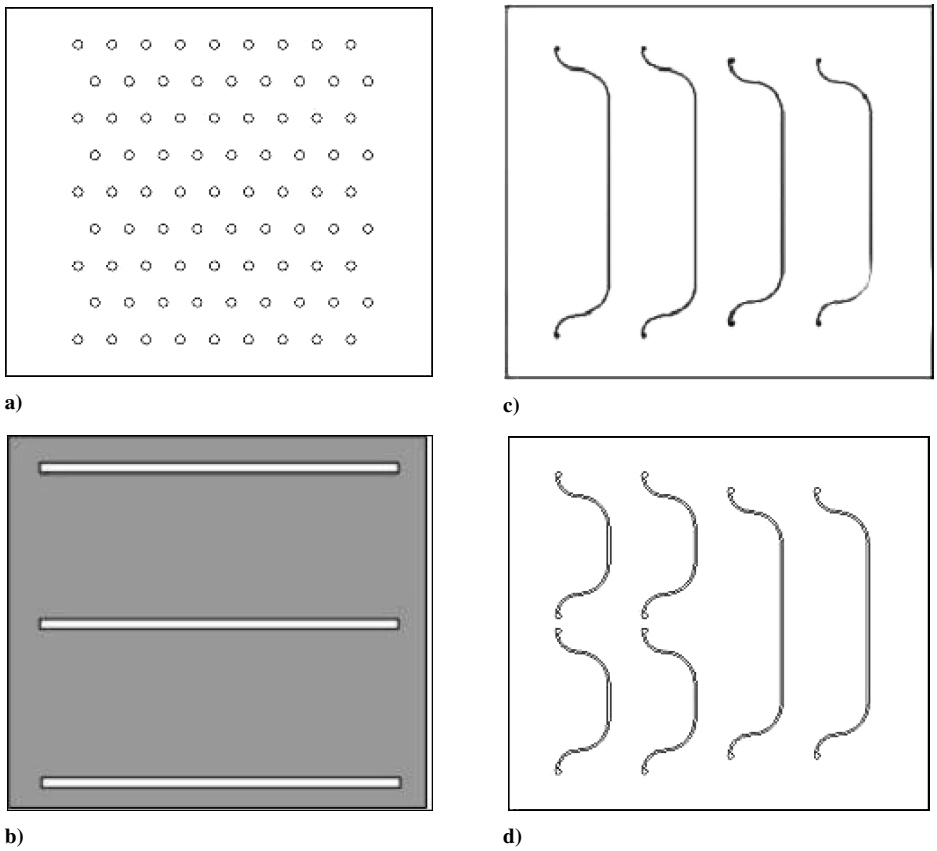

Fig. 2 Schematics of the various control devices: a) 5% macroporous plate, b) streamwise slots, c) conventional mesoflap array, and d) hybrid flap array.

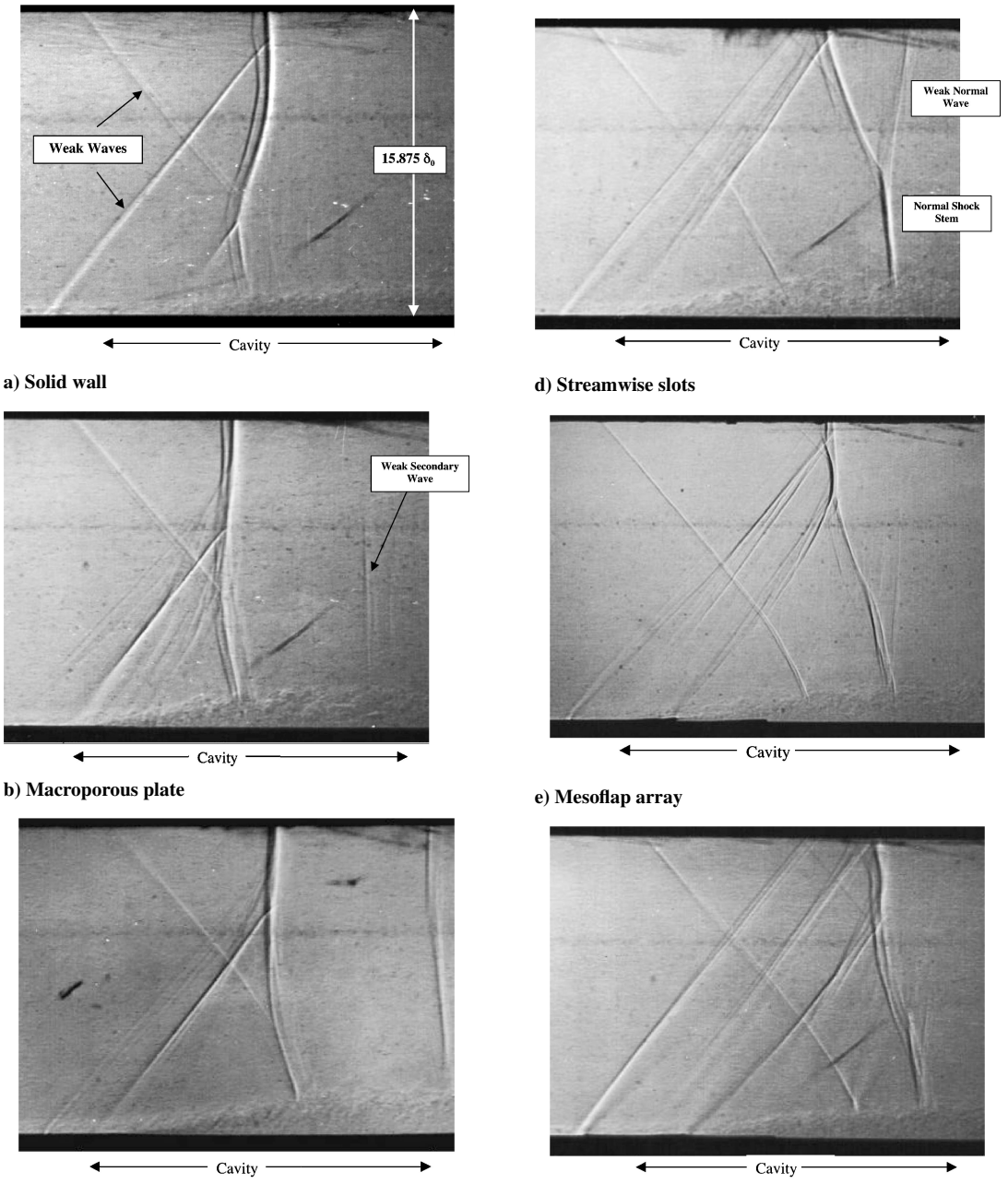

Fig. 3 Shadowgraphs of a) baseline solid wall, b) 5% macroporous plate, c) 4% microporous plate, d) streamwise slots, e) mesoflap array, and f) hybrid flap array.

Results

Shadowgraphs

The lower black surface in all of the shadowgraphs (Fig. 3) is the tunnel bottom wall. The top black surface (window frame) is 12.7 mm below the top wall. The flow is from left to right in all the shadowgraph pictures. Most of the shadowgraphs show a scratch in the lower right portion of the viewing window caused by the debonding of one of the flap arrays, and should not be interpreted as a flow feature.

Figure 3a shows the normal shock interaction with the solid wall. The boundary layer thickens sharply at the foot of the normal shock, resulting in a short leading oblique shock. The bifurcation point of the lambda structure is 4–5δ_0 above the bottom wall. The small triangular region of supersonic flow downstream of the leading oblique shock is terminated by the nearly normal trailing shock. A weak Mach wave (indicated by an arrow) can also be seen originating from the junction between the solid-wall insert and the bottom wall of the test section. A weak Mach wave from the top wall can also be seen entering the field of view. The origin of this wave is not clearly understood, but most likely results from imperfections in the C–D nozzle contour. In any event, this wave is weak in nature and hence does not significantly affect the flow.

Figure 3b depicts the SBLI occurring above the 5% macroporous plate. The extent of the cavity is shown in the figure. It can be observed that the shock is located slightly upstream of the middle of the cavity. This shock position was the most stable position[10,11] for macroporous plate control and was chosen for all the succeeding analyses. The weak Mach wave, originating from the junction of the bottom wall and the macroporous plate, is similar to that observed in Fig. 3a for the baseline solid wall. A number of weak waves can also be seen originating from the individual holes of the macroporous plate (just downstream of the leading oblique shock wave). A weak secondary normal shock is also observed in the flow downstream of

the SBLI, a phenomenon closely related to the behavior of classical shock trains.[16,17] It is also observed that the trailing shock of the lambda foot is approximately normal to the local boundary layer. The bifurcation point of the lambda shock is located 24.7 mm or $10.3\delta_0$ above the bottom wall, for the macroporous plate.

Figure 3c depicts the SBLI over the 4% microporous plate. The shock structure is similar to the SBLI observed over the 5% macroporous plate. A single large lambda shock is observed. The incoming Mach wave from the top wall bends relatively strongly toward the wall normal as it passes through the leading oblique shock, indicating the relative strength of this shock. Trailing weak normal waves in the transonic flow field downstream of the SBLI are also visible. The boundary layer thickens rapidly across the SBLI, and its downstream thickness is larger than for the 5% macroporous plate, as shown quantitatively by the LDV measurements to be presented below. The lambda-shock bifurcation point, located 27 mm ($11.3\delta_0$) from the bottom wall, is higher than for the macroporous plate.

Figure 3d presents the spanwise-integrated shadowgraph of the SBLI over the streamwise slots. A large normal shock-stem is positioned near the aft end of the cavity-streamwise center. This shock position was found to be the most stable for this control device, which is attributed to the recirculating flow pattern generated by the slots which caused a local peak in the displacement thickness, akin to a transonic bump. It is observed that, though the slots occupy only a small spanwise portion of the bottom wall, the resulting effect is global. A sharp change in the angle of the trailing normal shock is observed. The incoming Mach wave from the top wall bends strongly toward the wall normal as it passes through the leading oblique shock, again indicating the apparent strength of this shock. In addition, a weak normal wave, immediately downstream of the SBLI coalesces with the trailing normal shock of the lambda foot. However, the resulting effects of this latter interaction could not be determined. The bifurcation point of the lambda shock is located 36.6 mm or $15.3\delta_0$ above the bottom wall. As a result, the outgoing boundary layer thickens from 2.4 to 8.3 mm (behind the slots) across the SBLI (determined from the LDV measurements), which is thicker than for the rest of the control cases. It should be noted that the flowfield for the streamwise slots may be highly three-dimensional (i.e., strong spanwise variations as discussed later), making interpretation of the spanwise-integrated shadowgraph uncertain.

Figures 3e and 3f depict the SBLI over the mesoflap and hybrid flap arrays, respectively. The shock structure for these control cases is similar but is significantly different from that of the other control methods. Two distinct leading oblique shocks originate from the most upstream flap(s) due to (a) the opening of the flap to form a "ramp" that fixes the foot of the first leading oblique shock and (b) the injection of flow through the flap gap, which causes the formation of a stronger second oblique shock. It is observed that the second upstream/injection flap(s) has very small deflections. This could be due to small static pressure gradients across the flap. As a result, the second injection flap(s) does not form significant oblique shock structures (as seen for the most upstream flap(s)). The incoming Mach wave from the top wall bends more strongly toward the wall normal as it passes through the second oblique shock, revealing a larger change in Mach number for the second oblique shock. As expected, the small changes in flap shape and size for the hybrid flap arrays did not substantially affect the global shock structure of the flowfield. Weak normal waves are visible downstream of the cavity in both Figs. 3e and 3f. In addition, a sharp change in the angle of the trailing normal shock is observed, as it approaches the control surface for both cases. It should be noted that the shock position for the hybrid flap array is slightly more downstream than for the conventional mesoflap array. The lambda-shock bifurcation points for the mesoflap array and hybrid flap array controls are 29.9 mm ($12.5\delta_0$) and 27.9 mm ($11.6\delta_0$) above the bottom wall, respectively.

Surface Flow Visualizations

The solid wall surface flow visualization (Fig. 4a) indicates that a region of separation exists just downstream of the normal shock interaction, due to the pooling of oil ("separation region" in Fig. 4a) that occurs in this region. This feature is difficult to discern in Fig. 4a, but was more obvious when conducting the experiments. Separation of the flow just downstream of the normal shock stem is typical of flow fields with Mach numbers above 1.35 (Ref. 18). The flow is predominantly two-dimensional and becomes three-dimensional only near the sidewalls. The oil streaklines, upstream of the separated region, curve in from the sidewalls, toward the spanwise centerline, near the sidewalls.

Figure 4b depicts the surface oil-flow pattern for the 5% macroporous plate. The oil-flow pattern reveals very distinct flow features. The upstream holes of the macroporous plate inject the recirculated flow (from the cavity) transversely. The streamwise extent of separation in the flow field is difficult to assess as the flow exhibits three-dimensionality. The flow structure is consistent with observations of Orphanides.[11] The regions adjacent to the holes are not separated (probably due to the generation of streamwise vortices), and this trend is observed for all the holes across the span.

The surface oil-flow visualization of the streamwise slot control (Fig. 4c) reveals several remarkable flow features. The surface-flow patterns demonstrate the spanwise periodicity of the flowfield. The surface streaklines deflect away from the slots near the upstream part of each slot. The streaklines then return toward the slots and disappear into the rear end of the slots. This flow pattern indicates the presence of blowing in the upstream half of the slots and suction in the rear part of the slots. The streaklines around the slots indicate that blowing occurs through almost two-thirds of the length of the slot opening, while suction takes place only through the remaining one-third of the slot. The surface oil-flow patterns also indicate the presence of large spanwise deflections (velocities) near the control surface. The accumulation of oil on the surface also indicates regions of low-speed/separated flows. In the surface oil-flow pattern, the regions between the slots have low-speed/separated regions (see Fig. 4c), that is, low shear stresses, whereas the regions close to the slots have high shear stresses. It is believed that these regions of high shear stress are formed due to the presence of horseshoe vortices generated at the upstream end of the slots. It should also be noted that the flow does not separate in the vicinity of the slots, except immediately downstream of each slot. The surface oil-flow patterns discussed here are consistent with the observations of Smith et al.[9]

Schematics of the surface oil-flow over the mesoflap and hybrid flap arrays are shown in Figs. 4d and 4e, respectively. Sketches (and not photos) of the oil-streak patterns for the mesoflap and hybrid flap arrays are presented, since the steady-state patterns were altered during tunnel shutdown. The surface flow over the downstream flaps of the mesoflap and hybrid flap array controls are quite similar. The flow separation downstream of the normal shock, as encountered in the other control methods, is replaced by a region of low-speed flow since the low-momentum boundary layer downstream of the SBLI is bled off into the cavity. However, small separation zones are created near the S-curves of the upstream injection flaps (indicated by the shaded regions in Figs. 4d and 4e). Also, slow-moving oil on the surface of the third flap, indicates a region of low-speed flow in each case. In addition, the streaklines curve away from the spanwise center at the edges of the two upstream flaps but curve back toward the centerline at the two downstream flaps, indicating mass outflow from and inflow to the cavity, respectively.

Static Pressure Measurements

The surface static pressure distributions were measured for the baseline solid wall and the various control devices. Figure 5a shows the streamwise static pressure distribution on the spanwise centerline for the baseline solid wall and the different control devices. The streamwise location X^* is measured from the center of the cavity and is nondimensionalized with the incoming boundary layer thickness, that is, $X^* = (x - x_0)/\delta_0$. Static pressure is nondimensionalized by the tunnel stagnation pressure P_0.

As expected, the incoming static pressure distribution is essentially identical for all cases and is nearly constant spatially, although there is slight variation, most likely due to weak waves originating from the nozzle contour. The static-to-stagnation pressure ratio (for the baseline solid wall) P/P_0 is indicative of a freestream flow with a Mach number slightly lower than 1.41. The static pressure rises

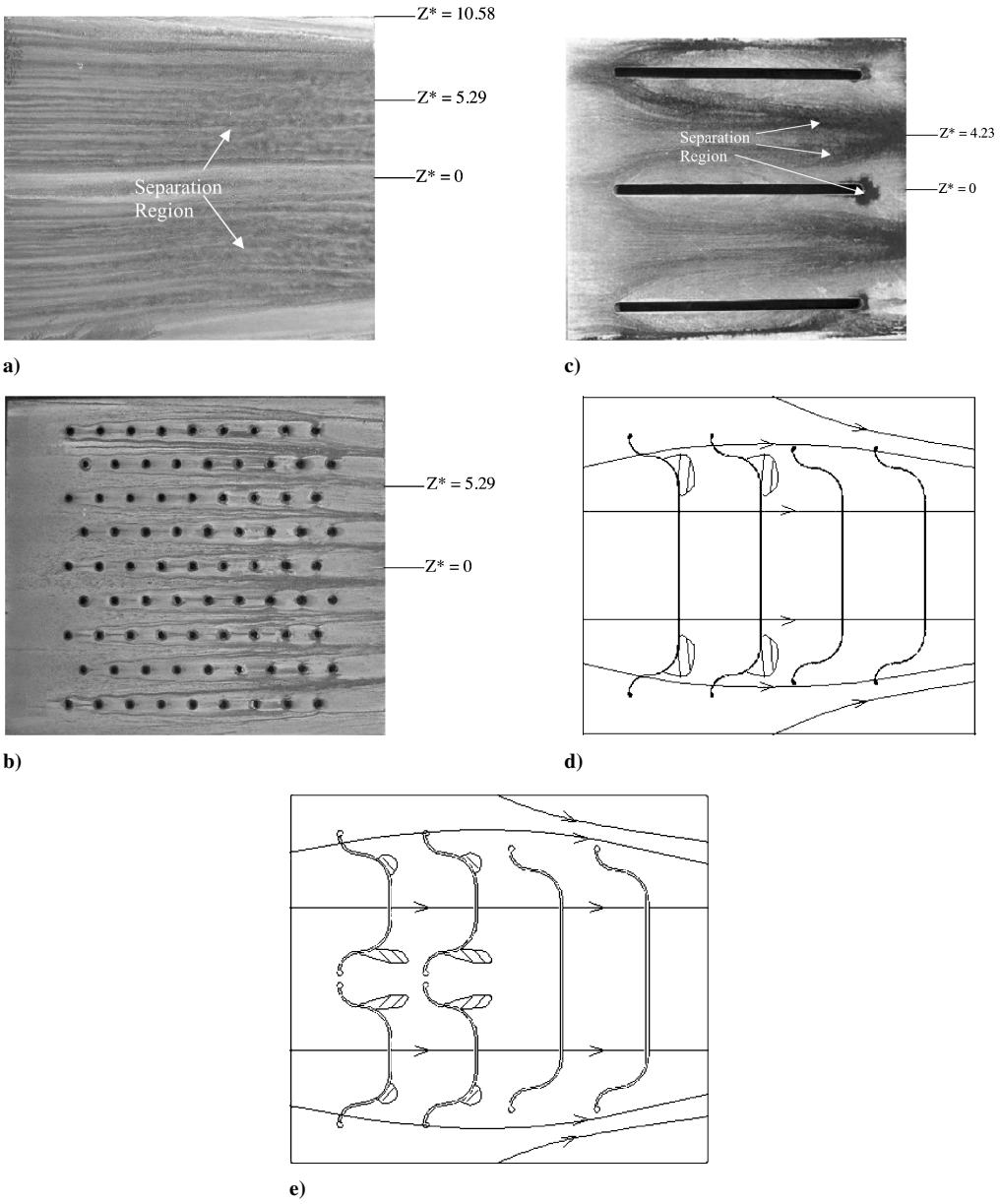

Fig. 4 Surface oil-flow visualization of a) baseline solid wall, b) 5% macroporous plate, c) streamwise slots, d) mesoflap array, and e) hybrid flap array.

across the shock interaction by a factor of approximately 1.9, compared to a factor of 2.15 predicted by idealized normal shock theory at Mach 1.41. The lower pressure rise is due to the presence of the two-dimensional oblique shock system, which is effectively weaker than a one-dimensional single normal shock. In addition, some of this effect can be attributed to flow acceleration downstream of the shock caused by the rapid thickening of the boundary layer.

In all recirculating flow cases, the static pressure is essentially constant throughout the cavity length, as found in previous studies.[5,9,19] In the cavity, the hybrid flap array and the 5% macroporous plate have the highest static pressures, whereas the streamwise slots have the lowest static pressure. The same trend can be observed downstream of the cavity. The 5% macroporous plate and the hybrid flap array have similar static pressure distributions. The baseline solid wall has downstream static pressures lower than most of the control devices, except for the streamwise slots and mesoflap array. It should be noted, though, that high static pressure values in the cavity, and subsequently downstream of the interaction, do not necessarily imply a high total pressure recovery (as will be shown later).

Figure 5b graphically depicts the spanwise variation of the static pressure at $X^* = 23.75$ for all six cases. The results indicate that the static pressure remains essentially constant across the span of the test section. The constancy of the spanwise static pressure distributions is used to calculate the total pressure maps (discussed later).

Boundary Layer Mean Velocity Profiles

The incoming flow had a freestream velocity of 418 m/s and an incoming boundary-layer thickness of 2.4 mm (Ref. 12). The incoming centerline mean boundary layer velocity profile is shown in Fig. 6. The velocity profile shape is consistent with that for fully developed, supersonic, turbulent boundary layers, and the thickness (2.4 mm) agrees qualitatively with shadowgraph pictures of the incoming flow. The incompressible displacement thickness, momentum thickness, and shape factor (δ^*, θ, and H) are 0.18 mm, 0.15 mm, and 1.2, respectively. The uncertainties associated with the evaluation of the incompressible displacement thickness, momentum thickness and shape factor are 23, 24, and 33%, respectively. Constant stagnation temperature was assumed to calculate an incoming freestream Mach number (from the velocity data) of 1.42, which agress well with the wall static pressure data. The uncertainty in the incoming Mach number is 2.1%.

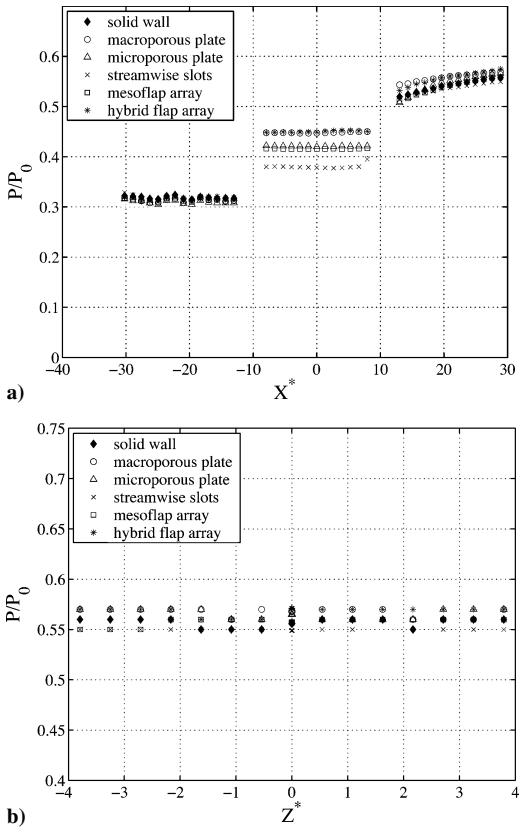

Fig. 5 Wall static pressure: a) streamwise centerline ($Z^* = 0$) and b) spanwise distributions at $X^* = 23.75$.

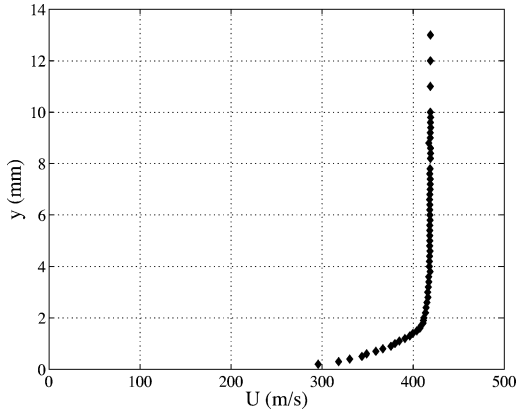

Fig. 6 Incoming centerline boundary-layer mean velocity profile measured at $X^* = -13$.

Spanwise Variation

The spanwise variation of the outgoing mean velocity profiles for the baseline solid wall and the various control devices at $X^* = 25$ is depicted in Fig. 7. The flowfield downstream of the SBLI over the baseline solid wall (see Fig. 7a) is predominantly two-dimensional. The mean velocity profile at $Z^* = 5.29$ shows the maximum extent of three-dimensionality in the flow over the current measurement domain. However, the three-dimensional effects are still relatively small, and it can be concluded that the overall flow downstream of the SBLI is predominantly two-dimensional for the baseline solid wall. The same trend is observed for the 5% macroporous and 4% microporous control devices (Figs. 7b and 7c).

The flowfield downstream of the SBLI for the streamwise slots (see Fig. 7d) is highly three-dimensional. The centerline of the center slot is aligned along $Z^* = 0$, whereas $Z^* = 4.23$ represents the symmetry plane between the center and off-center slots. It can be seen that there is significant spanwise variation in the velocity profiles at this streamwise location. The velocity profiles away from the slots ($Z^* = 3.175$ to 5.29) are considerably less full near the wall. The fullness of the boundary layer profiles behind the slots can be attributed to the presence of streamwise vortices. These vortices, generated by the slots, convect downstream and enable mixing of the flow. It is believed that the vortices generated by the slots influence the flow field in a manner similar to vortex generators. Also, the freestream velocity for all the spanwise locations is almost the same, suggesting that the three-dimensional features in the flow are restricted to locations within the boundary layer.

Figure 7e depicts the mesoflap array boundary-layer mean velocity profiles at $X^* = 25$. As observed for the baseline solid wall, the boundary-layer velocity profiles are predominantly two-dimensional. The more outboard velocity profiles ($Z^* = 4.23$ and 5.29) differ slightly from the rest of the spanwise profiles (i.e., slightly less full). It was observed that the ends of the upstream flaps (S-curves) deflect more than the inner portions. As a result, more of the incoming boundary layer is disturbed at the ends of the flaps. The $Z^* = 5.29$ plane is located directly behind the S-curves of the injection flaps (Fig. 2c). Hence, it is expected that the mean velocity profiles directly behind the S-curves ($Z^* = 5.29$) have thicker boundary-layer profiles. However, as the flow progresses downstream, the disturbances caused by the injection flaps die out, and the mean velocity profiles are quite two-dimensional.

For the hybrid flap array (Fig. 7f), as shown in the oil-streak schematics (see Fig. 4e), a separation region exists between $Z^* = 0$ and 1.06. As a result, the mean velocity profiles downstream of these locations suffer a velocity deficit away from the wall but only within the boundary layer. As expected, the mean velocity profiles away from the spanwise centerline are similar to the mean velocity profiles of the mesoflap array at this location. Note that measurements for the $Z^* = 5.29$ plane could not be obtained for either the microporous plate or hybrid flap array due to insufficient LDV oil-droplet seeding of the flow for these cases.

Streamwise Variation

Figure 8 depicts the streamwise evolution of the boundary layer mean velocity profiles for the baseline solid wall and the various control devices at $Z^* = 0$. For the baseline solid wall (see Fig. 8a), it is observed that the boundary layer thickens approximately threefold downstream of the SBLI, which is consistent with the shadowgraphs. A large decrease in the streamwise velocity component near the wall, compared to the incoming boundary layer, is indicative of the strong destabilization of the boundary layer downstream of the SBLI. This is consistent with the findings of Delery.[20] However, as the flow progresses downstream, the velocity near the wall begins to increase and the flow recovers. The redevelopment of the flow near the wall, coupled with the deceleration in the freestream is responsible for the crossing (intersection) of the mean velocity profiles near $Y^* = 2$. The velocity profiles downstream of $X^* = 13$ are approximately linear near the wall. This is consistent with wakelike behavior behind a region of separation.

Figure 8b depicts the streamwise evolution of the mean velocity profiles for the 5% macroporous plate at $Z^* = 0$. A deficit in the streamwise velocity is again observed near the wall at $X^* = 13$. As the flow progresses downstream, the flow recovers and the streamwise velocity deficit is reduced. As observed in the mean velocity profiles of the baseline solid wall, the mean velocity profiles for the 5% macroporous plate are approximately linear near the wall. Also, the velocity profiles at the different streamwise locations cross each other as the flow near the wall recovers and the freestream velocity decreases. The intersection point is unique and is located at about $Y^* = 1.2$.

Figure 8c depicts the streamwise variation of the mean velocity profiles for the 4% microporous plate at $Z^* = 0$. In this case, a large velocity deficit is observed in the mean velocity profiles near the wall. The boundary layer thickens, but the velocity profile becomes fuller near the wall as the flow progresses downstream. In addition, as observed for the baseline solid wall and the 5% macroporous plate, the streamwise profiles intersect at a unique location of approximately $Y^* = 1.75$. The freestream flow decelerates between

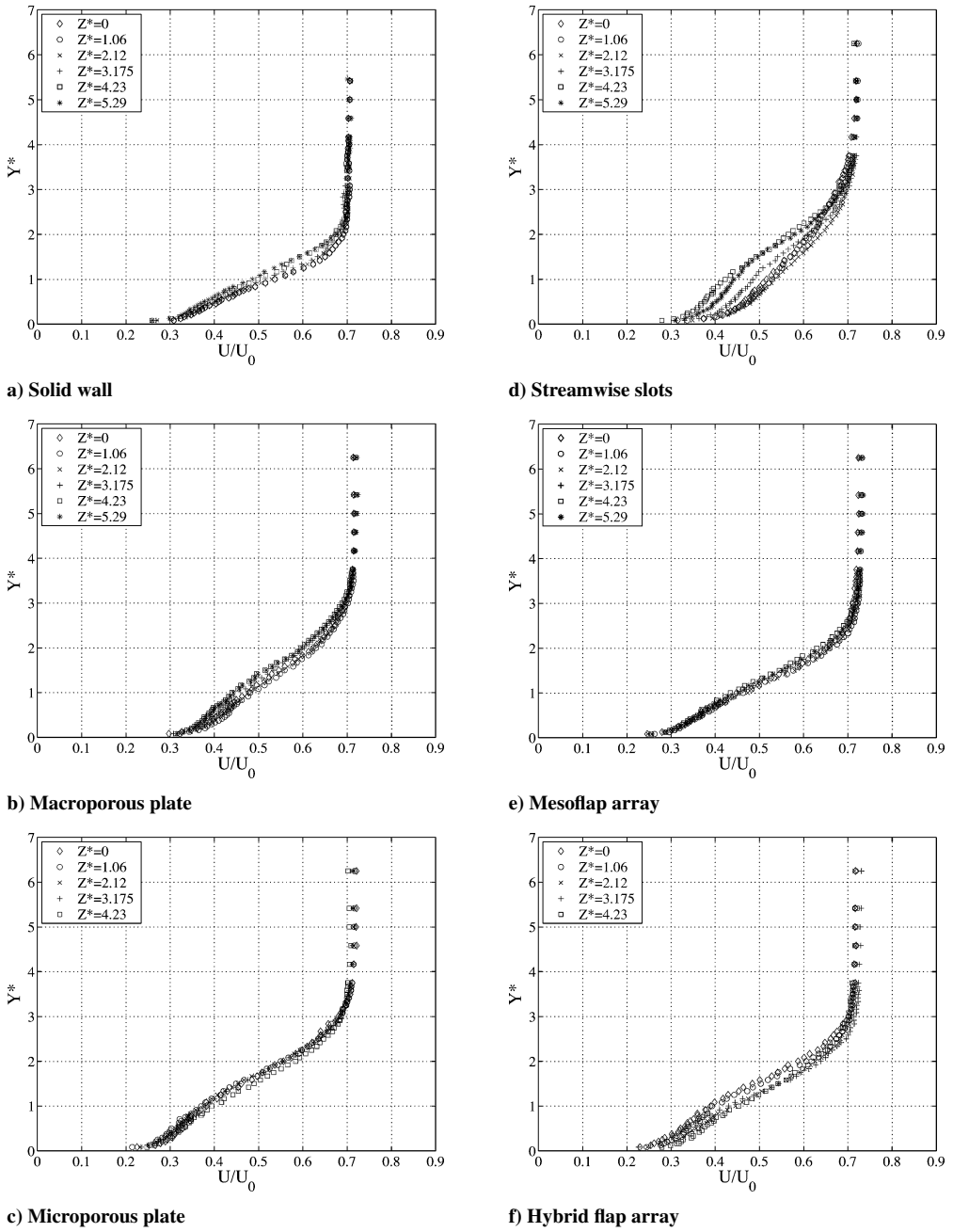

Fig. 7 Comparison of boundary layer mean velocity profiles at $X^* = 25$ for a) baseline solid wall, b) 5% macroporous plate, c) 4% microporous plate, d) streamwise slots, e) mesoflap array, and f) hybrid flap array.

$X^* = 13$ and 25, which is consistent with the streamwise static pressure increase in this range. The velocity profiles at $X^* = 25$ are less full compared to the velocity profiles of the baseline solid wall and the 5% macroporous plate at the same location.

Figure 8d depicts the streamwise variation of the mean velocity profiles for the streamwise slots at $Z^* = 0$. At the first streamwise measurement location ($X^* = 13$), the near-wall velocities for the mean velocity profiles are significantly lower than the near-wall velocities in the incoming mean velocity profile, indicating a strong destabilization of the boundary layer. The boundary layer behind the slots, $Z^* = 0$, is thicker but the velocity profile near the wall is fuller than for the baseline solid wall, particularly at $X^* = 13$. As the flow progresses downstream, the velocity profile becomes somewhat fuller near the wall, but the boundary layer becomes thicker. As seen in the mean velocity profiles for the baseline solid wall, the boundary-layer profiles for the streamwise slots also intersect at a unique location (approximately $Y^* = 1$ in this case).

Figures 8e and 8f depict the streamwise variation of the mean velocity profiles for the mesoflap and the hybrid flap arrays at $Z^* = 0$. The mean velocity profiles for the hybrid flap array immediately downstream of the SBLI, show a large velocity deficit near the wall. This trend is consistent with the presence of the flow separation near the centerline indicated in the oil-flow schematics (see Fig. 4e). The boundary layer recovery from the shock-induced separation is indicated by the increased fullness of the mean velocity profiles further downstream of the interaction for both the mesoflap and hybrid flap arrays.

Total Pressure Profiles

Figure 9 compares the mean velocity and near-field total pressure profiles of the baseline solid wall and the various control devices at $X^* = 25$ and $Z^* = 0$. As discussed earlier, the near-wall velocities for the streamwise slots at $Z^* = 0$ (Fig. 9a) are higher than in the other cases due to the generation of streamwise vortices at the beginning of each slot. It should also be noted that the freestream velocities for all the control cases are higher than that for the baseline solid wall, which is an outcome of the lambda foot benefit. Also, at $Z^* = 4.23$

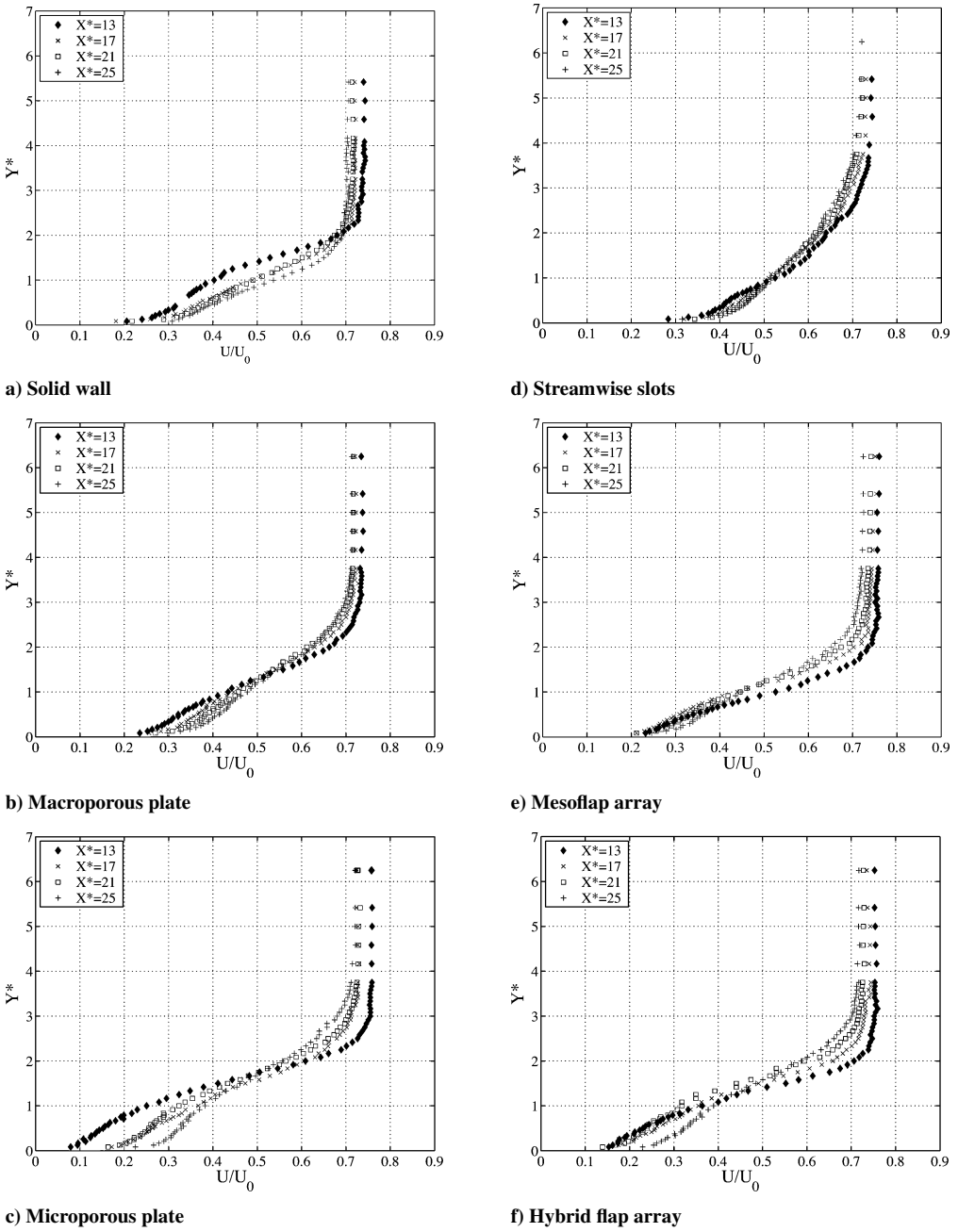

Fig. 8 Comparison of boundary layer mean velocity profiles at $Z^* = 0$ for a) baseline solid wall, b) 5% macroporous plate, c) 4% microporous plate, d) streamwise slots, e) mesoflap array, and f) hybrid flap array.

(Fig. 9b), the mean velocity profiles for the mesoflap and the hybrid flap arrays are similar, indicating that the mean velocity profiles (away from the spanwise centerline) of the hybrid flap array relax toward a shape similar to that for the conventional mesoflap array. A characteristic feature of the mean velocity profiles is the presence of a large velocity deficit in the boundary layer (for the various control devices relative to the solid wall) accompanied by a small velocity increase in the freestream.

The near-field total pressure distributions at $X^* = 13$–25 were not measured directly (e.g., with a pitot probe), due to potential probe-interference effects. However, they could be estimated from the boundary layer velocity measurements and the wall static pressure. Assuming a constant stagnation temperature, the Mach number could be computed from the measured velocity and adiabatic relations. Isentropic relations are then used to determine the local static-to-total pressure ratio P/P_t. If the downstream streamlines are approximately straight, and there is no interaction with a shock or expansion fan, it can be reasonably assumed that static pressure is constant across the boundary layer. Thus, total pressure profiles can be estimated using the local P/P_t ratio and the measured wall-static pressure (Fig. 5a). The uncertainity in the near-field total pressure estimations is 2.3%.

These total pressure profiles can be used to study the "lambda foot benefit" of the various devices. In Fig. 9c ($Z^* = 0$), the total pressure recovery between about $Y^* = 1$ and 2 is maximum for the baseline solid wall. However, the total pressure in the freestream for the various control devices is higher than that for the baseline solid wall. This is characteristic of flows with lambda shocks. The freestream total pressure is largest for the mesoflap array and lowest for the baseline solid wall. The freestream total pressure of the baseline solid wall is approximately 0.9 P_0, whereas the freestream total pressure of the mesoflap array is about 0.95 P_0. Note that the inviscid shock theory total-pressure ratio for an incoming Mach number of 1.42 (from LDV profiles) is 0.953.

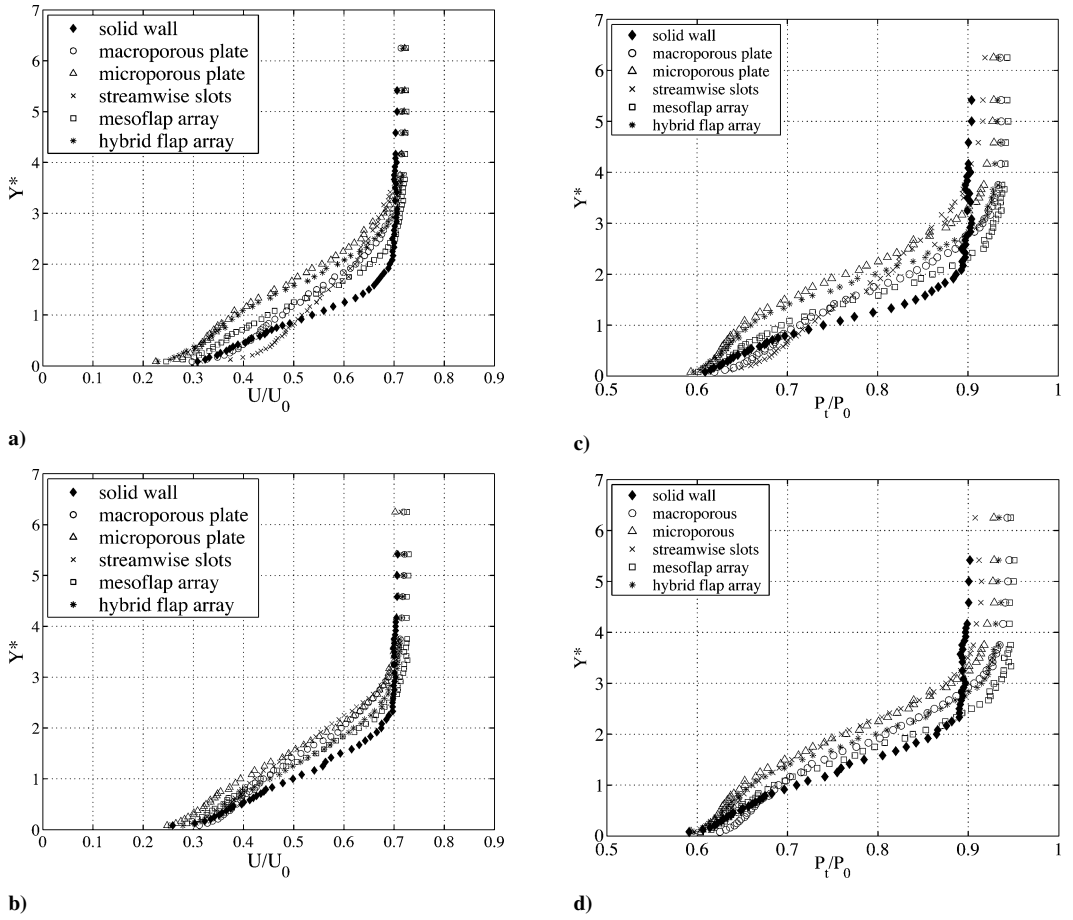

Fig. 9 Comparison of the most downstream ($X^* = 25$) mean velocity and near-field total pressure profiles at a) and c) $Z^* = 0$ and b) and d) $Z^* = 4.23$.

At $Z^* = 0$ (Fig. 9c), the near-wall total pressures for the streamwise slots are higher than for the baseline solid wall. These higher total pressures near the wall can be attributed to the fuller boundary-layer velocity profiles obtained downstream of the SBLI for the slots. Also, the total pressures in the freestream are higher for the streamwise slots than for the solid wall. However, the much thicker boundary layer for the streamwise slots generates larger viscous losses. At $Z^* = 4.23$ (Fig. 9b), the velocity profiles for the streamwise slots are less full compared to the velocity profiles at $Z^* = 0$. As a result, the near-wall total pressures are smaller than the baseline solid wall total pressures. Interestingly, at $Z^* = 4.23$ (Fig. 9d), the total pressures near the wall are similar for the baseline solid wall and the different control devices except the 5% macroporous plate, which has a higher near-wall total pressure (due to increased static pressure as noted in Fig. 5a).

The remainder of the control devices have similar trends for the total pressures. In the freestream, all of the control devices outperform the baseline solid wall. The freestream total pressure benefit is an outcome of reduced wave drag due to lambda shock formation. Near the wall, the control devices generally encounter higher viscous losses than for the solid wall. Overall, the mesoflap array was found to have a higher integrated mass-weighted total pressure than for the baseline solid wall. The integrated mass-weighted total pressure (α) is obtained by integrating the mass-weighted total pressures over the $X^* = 25$ cross-sectional plane normalized by the tunnel stagnation pressure P_0. These results will be discussed further below.

Figure 10 depicts the cross-stream (Y^*–Z^* plane) total pressure maps for the baseline solid wall and the different control devices at $X^* = 25$. The total pressure maps for the baseline solid wall, 5% macroporous plate, 4% microporous plate, and mesoflap array are predominantly two-dimensional. The contours of total pressure are also indicative of the relative boundary layer thicknesses and the viscous losses. For the streamwise slots, a large low-total pressure zone between $Z^* = 3.175$ and 5.29 is observed near the wall. This low total pressure zone is downstream of the low-speed/separated region indicated in the surface oil-flow visualization (see Fig. 4c). The low total pressure zone extends up to a Y^* of approximately 1.1, contributing largely to the lower stagnation pressure recovery (α) for this case.

Table 1 Stagnation pressure recovery of the different control methods[a]

Case	α	% Improvement	Extrapolated values ($Y^* = 0$–11.25)
Baseline solid wall	0.840	0.0	0.0
5% Macroporous plate	0.835	−0.5	−0.9
4% Microporous plate	0.811	−3.4	−3.3
Streamwise slots	0.836	−0.4	−0.6
Mesoflap array	0.849	1.0	0.6
Hybrid flap array	0.826	−1.6	−0.8

[a]Based on mass-weighted integrated total pressure profiles at $X^* = 25$ ($Y^* = 0$–6, $Z^* = 0$–4.23) and also extrapolated values ($Y^* = 0$–11.25).

To summarize the total pressure maps, the mass-weighted total pressure recovery at $X^* = 25$ is presented in Table 1. Because the velocity for all cases did not vary significantly above $Y^* = 4$ (Figs. 7 and 8), the total pressure profiles were also extrapolated from $Y^* = 6.25$ to $Y^* = 11.25$ to cover the entire lambda-shock region for each case, and the results are listed in Table 1. The different control methods described above work on the same fundamental concept of reducing the wave drag (through a lambda shock). However, the reduction in wave drag is usually accompanied by an increase in viscous drag (through thicker boundary layers). An optimum balance exists between the two opposing tendencies. In the present study, only the mesoflap array was found to outperform the baseline solid wall for the near-field integrated total pressure (see Table 1). Although the increase is small, it is significant for supersonic inlet

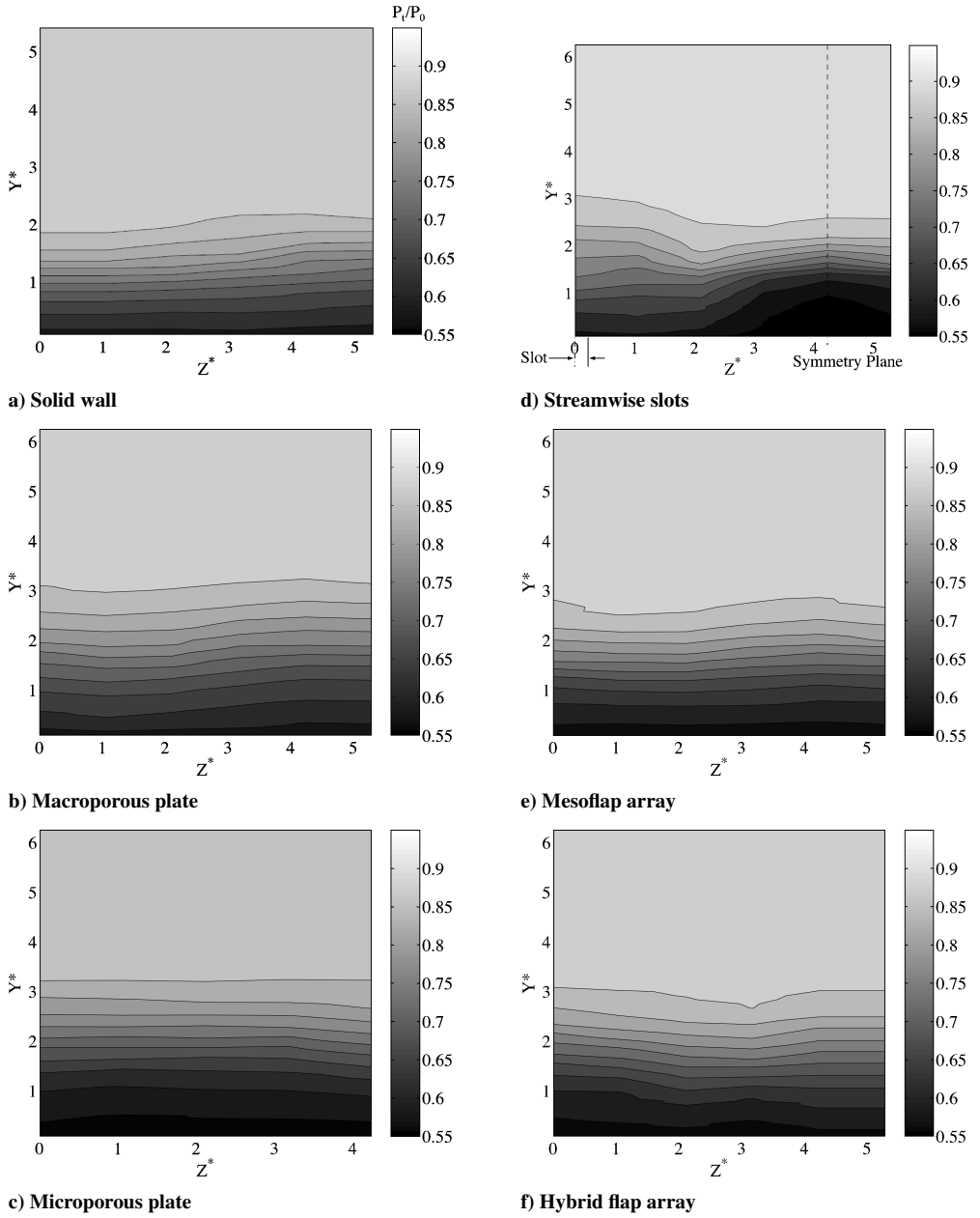

Fig. 10 Total pressure maps at $X^* = 25$ for a) baseline solid wall, b) 5% macroporous plate, c) 4% microporous plate, d) streamwise slots, e) mesoflap array, and f) hybrid flap array.

applications. Note that quantitative evaluation of flow distortion was not obtained because the present measurements did not cover the entire cross-section to the side-walls. However, the flow downstream of the three-dimensional devices (streamwise slots and hybrid flap array) tended to have larger distortions.

Boundary-Layer Integral Properties

The incompressible boundary-layer parameters (δ^*, θ, and H) were numerically integrated from the mean velocity profiles. The displacement thicknesses were normalized by the incoming displacement thickness of 0.181 mm. Figure 11a graphically depicts the spanwise variation of the normalized displacement thicknesses at $X^* = 25$ for the baseline solid wall and all the control devices. As expected, only the streamwise slots and the hybrid flap array show significant three-dimensional effects (i.e., spanwise variations). As observed in the total pressure maps of the streamwise slots, the flow downstream of the separated region ($Z^* = 4.23$) is the slowest to recover, and hence has higher displacement thicknesses. At this $X^* = 25$ location, the 4% microporous plate has the largest displacement thicknesses, and thus probably suffered the strongest destabilization of the boundary layer (among the control devices).

The downstream momentum thicknesses (Fig. 11b) are normalized by the incoming momentum thickness of 0.152 mm. As observed in the displacement thicknesses plots, the 4% microporous plate generally has the highest momentum thicknesses at $X^* = 25$, indicating higher friction drag over the extent of the interaction domain. Note that the baseline solid wall has the lowest momentum thicknesses (and displacement thicknesses; Fig. 11a) at this location, thus incurring the lowest friction drag over the interaction domain.

The shape factor, $H = \delta^*/\theta$, provides a measure of the resistance of the boundary layer to separation. Figure 11c graphically depicts the spanwise shape factor variation of the baseline solid wall and the various control devices at $X^* = 25$. Interestingly, the 5% macroporous plate and the streamwise slots (near $Z^* = 0$) have shape factors lower than for the baseline solid wall. It is to be noted, however, that the displacement and momentum thicknesses for the 5% macroporous plate are significantly higher than that of the baseline solid wall. The streamwise slots have the lowest overall shape factors, perhaps confirming the presence of streamwise vortices and their subsequent role in energizing the boundary layer.

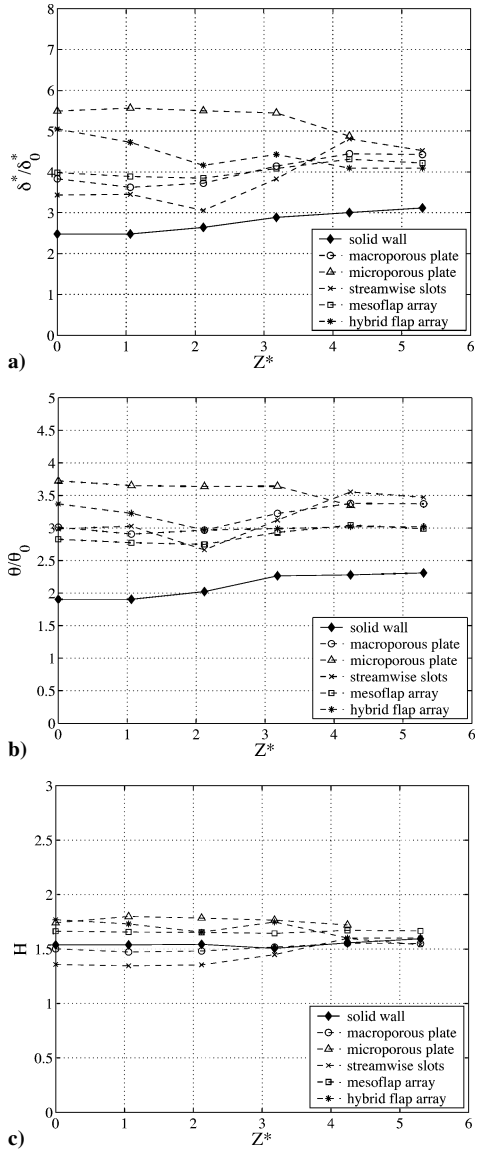

Fig. 11 Comparison of the spanwise variation of boundary layer integral properties at $X^* = 25$: a) displacement thickness, b) momentum thickness, and c) shape factor.

Table 2 Stagnation pressure recovery of the different control methods[a]

Case	α	% Improvement
Baseline solid wall	0.931	0.0
5% Macroporous plate	0.930	−0.1
4% Microporous plate	0.929	−0.2
Streamwise slots	0.917	−1.5
Mesoflap array	0.933	0.2
Hybrid flap array	0.932	−0.1

[a]Based on centerline mass-weighted pitot pressure profiles measured in the subsonic diffuser ($X^* = 102.5$, $Z^* = 0$).

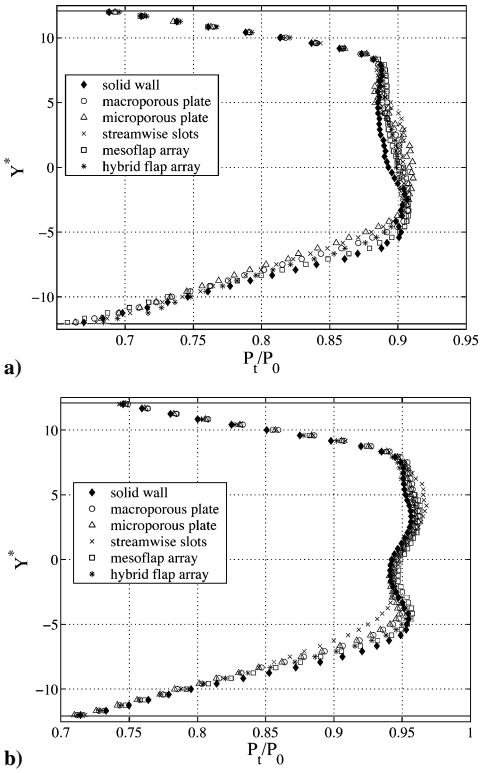

Fig. 12 Total pressure profiles for the different control methods measured in the subsonic diffuser ($X^* = 102.5$) a) along centerline ($Z^* = 0$) and b) off-center ($Z^* = 4.65$).

Diffuser Stagnation Pressure Measurements

Stagnation pressure profiles, measured in the downstream subsonic diffuser with a pitot probe, are shown in Fig. 12. As observed with the near-field total pressure distributions determined from the LDV profiles and static pressure measurements, the baseline solid wall has the highest stagnation pressures close to the bottom wall (above about $Y^* = -10$); see Fig. 12a at $Z^* = 0$ and Fig. 12b at $Z^* = 4.65$. As expected, the streamwise slots have the lowest stagnation pressures in this region, a result of the thicker boundary layers downstream of the SBLI. The most noteworthy aspect of the profiles is the freestream region. Every control case has a clear lambda-foot benefit region. Thus, all the control devices have higher stagnation pressures in the freestream, a benefit obtained due to the reduced wave drag. The streamwise slots extract the maximum lambda-foot benefit near the upper wall. This could be attributed to the larger lambda shock, as observed for the slots in the shadowgraphs. However, the large lambda shocks are also responsible for the slots' poor performance in the boundary layers. The stagnation pressure profiles thus emphasize the importance of the right balance between the viscous boundary-layer losses and the reduced wave drag gains.

A good indicator of the performance of the different control devices is the integrated stagnation pressure recovery factor, α. The stagnation pressure recovery factor is determined as the integrated mass-weighted normalized stagnation pressure recovery in the diffuser. The stagnation pressures are normalized by the operating tunnel stagnation pressure P_0. The stagnation pressure recovery factors along the centerline, for the different cases are presented in Table 2. Only the mesoflap array has a higher integrated recovery factor than for the baseline solid wall. This result is consistent with the results obtained in the near field using the LDV velocity profiles (Table 1). However, note that the LDV traverses do not span the entire height of the tunnel. Hence, direct comparisons of α between the two locations should be done cautiously.

The off-center pitot pressure profiles in the subsonic diffuser are shown in Fig. 12b. The off-center total pressure profiles are apparently influenced by the sidewall boundary layers. As a result, the lambda-foot benefit seen in the centerline total pressure profiles is not present as strongly in the off-center measurements. Table 3 gives the integrated off-center total pressure recovery for the baseline solid wall and the different control methods. As observed in the centerline total pressure profiles, the mesoflap array is the only control device that achieves an integrated stagnation pressure recovery that is higher than for the baseline solid wall. As in the near field, the total pressure recovery improvements are small but significant for supersonic inlet applications.

Table 3 Stagnation pressure recovery of the different control methods[a]

Case	α	% Improvement
Baseline solid wall	0.905	0.0
5% Macroporous plate	0.903	−0.2
4% Microporous plate	0.901	−0.4
Streamwise slots	0.902	−0.3
Mesoflap array	0.907	0.2
Hybrid flap array	0.903	−0.2

[a]Based on off-center mass-weighted pitot pressure profiles measured in the subsonic diffuser ($X^* = 102.5$, $Z^* = 4.65$).

Conclusions

Experiments have been performed for a normal shock/boundary-layer interaction with various types of passive control devices. Five different control devices were examined and their aerodynamic performance was compared to that for the baseline solid wall. It was found that all the control devices gave rise to larger lambda shocks than for the baseline solid wall. All of the control devices also had stronger destabilizations of the boundary layer than for the baseline solid wall, a characteristic feature of passive control devices. It was found that the flowfield downstream of the macroporous, microporous, and mesoflap array is predominantly two-dimensional, whereas the flowfield downstream of the streamwise slots and hybrid flap arrays is three-dimensional.

The mesoflap array was found to have the largest near-field and far-field stagnation pressure recovery (α). The shadowgraph for this case indicates formation of a larger lambda shock than for the baseline solid wall. Also, the surface oil-flow visualizations suggest substantial reduction of flow-separation downstream of the SBLI for this case. The flowfield downstream of the SBLI over the streamwise slots is highly three-dimensional. The boundary-layer profiles directly behind the slots increase in fullness and have lower shape factors than for the baseline solid wall, thereby showing more resistance to separation. The conventional passive control devices (5% macroporous and 4% microporous plates) did not perform nearly as well as the mesoflap array. To combine the benefits of the mesoflap array (increased stagnation pressure recovery) and the streamwise slots (improved boundary layer health), hybrid flap arrays were designed. However, the flow downstream of the S-curves did not experience the same benefits as for the streamwise slots. It is hypothesised that the streamwise vortices generated from the flap edges have lower strengths compared to the slots and hence do not energize the boundary layers as desired.

The results generally confirm that tangential injection/bleed-type passive control devices (i.e., flap arrays) generally outperform the more conventional transverse blowing/suction devices. However, in spite of transverse suction/blowing, the streamwise slots had fuller boundary layers directly behind the slots presumably due to the presence of streamwise vortices. This result strongly encourages the study of control devices that combine tangential injection/bleed with vortex generators.

References

[1]Gridley, M., and Walker, S., "Advanced Aero-Engine Concepts and Controls," AGARD CP 572, 1996.

[2]Bahi, L., Ross, J., and Nagamatsu, H., "Passive Shock-Wave/Boundary-Layer Control for Transonic Airfoil Drag Reduction," AIAA Paper 83-0137, Jan. 1983.

[3]Raghunathan, S., "Passive Control of Shock-Boundary Layer Interaction," *Progress in Aerospace Sciences*, Vol. 25, No. 3, 1988, pp. 271–296.

[4]Raghunathan, S., and McIlwain, S., "Further Investigations of Transonic Shock-Wave Boundary-Layer Interaction with Passive Control," *Journal of Aircraft*, Vol. 27, No. 1, 1990, pp. 60–65.

[5]Bur, R., and Corbel, B., and Delery, J., "Study of Passive Control in a Transonic Shock Wave/Boundary-Layer Interaction," *AIAA Journal*, Vol. 36, No. 3, 1998, pp. 394–400.

[6]Bur, R., Benay, R., Corbel, B., and Delery, J., "Physical Study of Shock-Wave/Boundary-Layer Interaction Control in Transonic Flow," AIAA Paper 2000-0933, Jan. 2000.

[7]McCormick, D., "Shock/Boundary-Layer Interaction Control with Vortex Generators and Passive Cavity," *AIAA Journal*, Vol. 31, No. 1, 1993, pp. 91–96.

[8]Lin, Y., Rimlinger, M., Shih, T., and Willis, B., "Control of Shock-Wave/Boundary-Layer Interactions with Passive Blowing and Bleeding," AIAA Paper 97-3002, July 1997.

[9]Smith, A., Babinsky, H., Fulker, J. L., and Ashill, P. R., "Shock Wave/Boundary-Layer Interaction Control Using Streamwise Slots in Transonic Flows," *Journal of Aircraft*, Vol. 41, No. 3, 2004, pp. 540–546.

[10]Hafenrichter, E., Lee, Y., Dutton, J., and Loth, E., "Normal Shock/Boundary-Layer Interaction Control Using Aeroelastic Mesoflaps," *Journal of Propulsion and Power*, Vol. 19, No. 3, 2002, pp. 464–472.

[11]Orphanides, M., "Passive Control of Normal Shock/Boundary Layer Interaction Using Aeroelastic Mesoflaps," M.S. Thesis, Dept. of Mechanical and Industrial Engineering, Univ. of Illinois, Urbana, IL, 2003.

[12]Srinivasan, K., Loth, E., and Dutton, J., "Aerodynamics of Recirculating Flow Control Devices for Normal Shock/Boundary Layer Interactions," AIAA Paper 2004-0426, Jan. 2004.

[13]Settles, G., and Teng, H., "Flow Visualization Methods for Separated Three-Dimensional Shock Wave/Turbulent Boundary-Layer Interactions," *AIAA Journal*, Vol. 21, No. 3, 1983, pp. 390–397.

[14]Bloomberg, J., "An Investigation of Particle Dynamics Effects Related to LDV Measurements in Compressible Flows," M.S. Thesis, Dept. of Mechanical and Industrial Engineering, Univ. of Illinois, Urbana, IL, 1989.

[15]Amatucci, V., "An Experimental Investigation of the Two Stream, Supersonic, Near-Wake Flowfield Behind a Finite-Thickness Base," Ph.D. Dissertation, Dept. of Mechanical and Industrial Engineering, Univ. of Illinois, Urbana, IL, 1990.

[16]Carroll, B., "A Numerical and Experimental Investigation of Multiple Shock Wave/Turbulent Boundary Layer Interactions in a Rectangular Duct, Ph.D. Dissertation, Dept. of Mechanical and Industrial Engineering, Univ. of Illinois, Urbana, IL, 1988.

[17]Carroll, B., and Dutton, J., "Characteristics of Multiple Shock Wave/Turbulent Boundary-Layer Interactions in Rectangular Ducts," *Journal of Propulsion and Power*, Vol. 6, No. 2, 1990, pp. 186–193.

[18]Seddon, J., "The Flow Produced by Interaction of a Turbulent Boundary Layer with a Normal Shock Wave of Strength Sufficient to Cause Separation," British Aeronautical Research Council, Repts. and Memoranda 3502, London, March 1960.

[19]Gefroh, D., Hafenrichter, E., Ford, B., Dutton, J., McIlwain, S., and Loth, E., "Experimental Study of Mesoflaps for SBLI Control," AIAA Paper 2000-0355, Jan. 2000.

[20]Delery, J., "Experimental Investigation of Turbulence Properties in Transonic Shock/Boundary-Layer Interactions," *AIAA Journal*, Vol. 21, No. 3, 1983, pp. 180–185.

R. So
Associate Editor